Laminar to Turbulence Transition in Boundary Layers due to Tripping Devices

P. Balakumar
Flow Physics and Control Branch, NASA LaRC, MS 170, Hampton, VA 23681-2199
Email: ponnampalam.balakumar-1@nasa.gov, (757) 864-8453

Prahladh S. Iyer
National Institute of Aerospace, Hampton, VA 23666

Abstract

Direct numerical simulations (DNS) and linear stability analyses were performed to identify the mechanisms by which two- and three-dimensional trips promote early transition in subsonic boundary layers over a flat plate. Investigations were conducted for three boundary-layer transition trip configurations: a two-dimensional smooth hump, a two-dimensional rectangular-shaped rod and a three-dimensional zig-zag tape. The smooth hump was used by Park et al.[1] in the linear and nonlinear parabolized stability (PSE) computations. Reynolds numbers based on the trip heights are 710, 683, and 300 for the two- and three-dimensional trips, respectively. Simulations with the smooth hump showed that the flow becomes stable upstream and strongly unstable downstream of the hump. Simulations with the two-dimensional rectangular trip showed that the flow separates at the top of the trip and forms a long recirculation zone downstream. However, the flow remains steady in the simulation without any external disturbances. Linear stability analysis showed that the inflectional profile in the recirculation zone is strongly unstable to frequencies in the range of 100-300 *Hz*. Simulations with the external disturbances forced at the frequency of 200 Hz showed that disturbances grow strongly inside the recirculation zone as observed in the Klebanoff[2] experiment. Three-dimensional simulations with secondary disturbances of fundamental, subharmonic, and oblique types produced turbulent flows shortly downstream. The three-dimensional zig-zag trip with a small roughness Reynolds number lead to early breakdown to a turbulent flow.

I. Introduction

Tripping devices are generally used to fix the boundary-layer transition from laminar to turbulent flow in wind tunnel experiments. This makes the flow over the experimental model fully turbulent starting downstream of the trip and enables the experimental data to be extrapolated to flight conditions. Several trip types are used in wind tunnel experiments, including two-dimensional rods, sand-grains, and rows of cylindrical disks or spherical particles. The trip heights are selected based on correlation data collected from several experimental data sets.[3] The commonly used parameter is the critical roughness Reynolds number $Re_{kk} = U_k k/\nu_k$, where k is the roughness height, and U_k and ν_k are the undisturbed boundary-layer velocity and the kinematic viscosity at the roughness height, respectively. A critical value of $Re_{kk} = 600$ was suggested based on experimental data.

Surface trips basically modify the incoming boundary layer and make the flow downstream more unstable. Klebanoff et al.[2, 4] performed detailed experimental investigations of the mechanisms involved in two- and three-dimensional roughness-induced transition in incompressible flows. Tani[5] reviewed experimental findings of roughness induced transition in flat plate boundary layers. They found that two-dimensional roughness elements cause early transition, compared to that without roughness, due to the destabilizing influence of the inflectional boundary-layer profiles behind the roughness. They also demonstrated that the upstream movement of the transition point towards the roughness is gradual with increasing Reynolds number. An important finding in the transition induced by a three-dimensional roughness element is that after a critical Reynolds number, the transition front moves rapidly towards the roughness element with a small increase in Reynolds number. The critical roughness Reynolds number for a hemispherical roughness was $Re_{kk} = 325$. The critical Reynolds number was 450 for a cylindrical element. Detailed hot-wire measurements in the vicinity of the roughness element showed the existence of well-defined periodic disturbances downstream of the roughness element. It was postulated that the flow field immediately behind the roughness consists of waves, and these waves change to hairpin vortices downstream. With increasing velocity, the

shedding of hairpin vortices starts immediately downstream of the roughness. These observations agree with the flow visualization studies of Acarlar and Smith.[6]

In Direct Numerical Simulations (DNS) and Large-Eddy Simulations (LES), one has to introduce consistent turbulent fluctuations at the inflow or at some station close to the inflow of a computational domain, to achieve a fully developed turbulent flow in a short distance from the inflow plane, except in periodic domains.[7] In multizonal hybrid Reynolds-averaged Navier-Stokes (RANS)/LES methods, one has to generate turbulence at the RANS-to-LES interface to change the flow from one state to another. One method is to generate synthetic turbulence at the interface[7] and the other is to trip the boundary layer. Tripping in numerical simulations is not as simple as in the wind tunnel experiments. In the wind tunnel experiments, freestream turbulence in the tunnel initiates the instabilities downstream of the trip and causes the flow to become turbulent. In simulations, the numerical noise may not be sufficient to initiate the instabilities, particularly in higher-order methods, and additional external forcing may be necessary to trigger the instabilities in the flow. Hence, understanding the mechanisms and identifying the important parameters that cause the flow behind the trips to become turbulent are very important.

Laminar-to-turbulent transition behind two-dimensional roughness from laminar to turbulent state occurs due to evolution and interaction of different disturbances inside the shear layer that forms at the roughness. Initially the unsteady disturbances in the freestream, such as turbulence, generate instability waves inside the boundary layer. The amplitudes of these disturbances grow exponentially downstream and reach large values. In the next stage, these large amplitude waves become unstable to three-dimensional waves. This is called secondary instability and beyond this stage the spectrum broadens, due to complex interactions and further instabilities, and the flow becomes turbulent in a short distance downstream. In this paper, this route to turbulence behind two-dimensional trips is investigated to determine the effectiveness of trips in causing early transition.

The secondary instability analysis of two-dimensional boundary layers is reviewed by Herbert (1988).[8] In the secondary instability analysis, a three-dimensional wave with a particular wavelength and a frequency is superimposed onto the primary instability wave and a Floquet analysis is performed to determine the growth of the three-dimensional secondary wave. There exist two types of secondary instability waves. One is the fundamental mode and the second is the subharmonic mode. In the fundamental mode the frequency of the secondary wave is the same as the primary wave and in the subharmonic mode the frequency is half of the primary wave. The spanwise wavelength of the secondary wave is on the order of the wavelength of the primary wave. There exist a large number of secondary instability analyses using Floquet analysis,[8] nonlinear PSE,[9, 10] and direct numerical simulations.[11, 12] In addition to fundamental and subharmonic breakdown mechanisms, the oblique breakdown mechanism is also considered as a viable path to transition in boundary layers.[13, 14, 15, 16] In oblique mode type breakdown, two symmetric oblique modes with a particular frequency and wavelength are superimposed into the mean flow. The two oblique modes interact and generate a steady streamwise vortex. The amplitude of the vortex grows and leads to breakdown. The simulations of different breakdown mechanisms are performed by applying harmonic sources through a slit upstream of the two-dimensional trips.

The objective of the present research is to study the effectiveness of trips in causing transition to turbulence using numerical simulations, by identifying the two- and three-dimensional stability characteristics of the modified boundary-layer profiles downstream of the trips. After identifying the possible mechanisms, an analysis will be performed to investigate whether the boundary-layer transition can be enhanced by external forcing. This will facilitate an efficient tripping strategy in computational simulations of turbulent flow over aerodynamic bodies.

II. Models and Flow Conditions

Computations are performed for flows over a flat plate. The schematic diagram of the computational domain is depicted in Fig. 1. The x, y, and z axes are aligned in the streamwise, wall normal, and spanwise directions, respectively. The inflow of the computational domain is located at a distance x_o from the leading edge of a flat plate and the center of the roughness element is located at a distance x_r from the leading edge. Simulations are performed for two types of two-dimensional roughness trips and for one three-dimensional zig-zag trip.

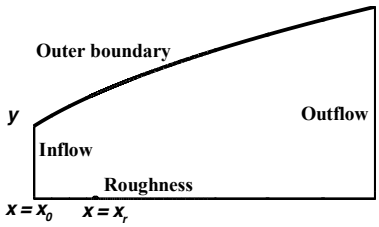

Fig. 1 Schematic diagram of the computational setup.

(a) Two-dimensional smooth hump

One of the two-dimensional trips is a smooth hump defined by a third-order polynomial. This shape was used by Park et al.[1] in their linear and nonlinear stability analysis of flows over smooth humps using Parabolized Stability Equations (PSE). The shape of a two-dimensional smooth hump is defined by the following equation.

$$h(x,z) = k\, f(t) \tag{1}$$

where

$$t = \frac{(x-x_r)}{b} \quad \text{and} \tag{2}$$

$$f(t) = 1 - 3t^2 + 2|t|^3 \quad \text{for } |t| \le 1 \tag{3}$$

Here, k is the height, b is the half width of the hump, and x_r is the coordinate of the center of the trip. A schematic diagram of a smooth hump is shown in Fig. 2(a). Simulations are performed at a unit Reynolds number based on the freestream velocity, density, and temperature of $Re = \rho_\infty U_\infty / \mu_\infty = 1*10^6$ m^{-1}. The freestream Mach number is M = 0.2, and the freestream temperature is $T_\infty = 300$ K. The inflow boundary is located at $x_o = 0.1m$ and the center of the roughness is located at $x_r = 1m$. The half width of the hump is selected to be $b = 0.1x_r$ and the height of the hump at the peak point is k=0.015b. The parameters used are the same as used by Park et al.[1] except that the PSE analysis were performed for incompressible flow. The undisturbed boundary-layer profile at the trip location is also drawn in Fig. 2(a). The boundary-layer thickness at this location is δ =0.0062 m. The ratio of the trip height to the boundary layer thickness is about k/δ= 0.25. The variation of the roughness Reynolds number, $Re_{kk} = U_k\, k/\nu_k$, along the boundary layer height is shown in Fig. 2(b). The roughness Reynolds number for this roughness height k = 0.0015 is about 760.

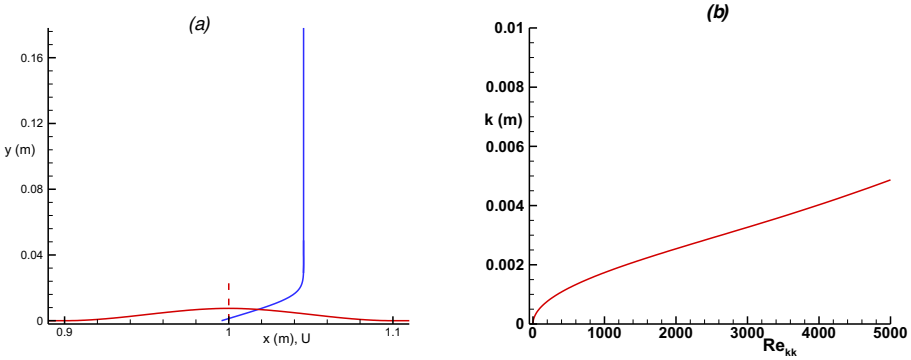

Fig. 2 The shape of a two-dimensional smooth hump. (a) cross sectional view across the hump and the boundary layer profile (not to scale), and (b) variation of the roughness Reynolds number, Re_{kk}.

(b)Two-dimensional rod

The shape of a two-dimensional rectangular rod is given by the following equation

$$h(x,z) = k\,\{0.5 - 0.5\tanh\{\sigma\,(r - r_0)/\Delta r\}\} \tag{4}$$

where

$$r = abs(x - x_r). \tag{5}$$

Here, k is the height, r_0 is the half width of the trip, and x_r is the coordinate of the center of the trip. The parameters σ and Δr determine the smoothness of the roughness element at the edges and they are selected to be 4 and 0.5r_0,

respectively. Simulations were performed at different heights and widths and the results are presented in this paper for a trip height of $k = 0.0132\ m$ and a width of $r_0 = 2k$. Simulations are performed at a unit Reynolds number based of $Re = 68{,}050\ m^{-1}$. The freestream Mach number is $M = 0.2$, and the freestream temperature is $T_\infty = 300$ K. The inflow boundary is fixed at $x_0 = 1$m and the center of the roughness is placed at $x_r = 2.086m$. These parameters yield the Reynolds numbers based on displacement thickness at the inflow as 450 and at the roughness location as 650. The Reynolds number at the inflow matches the Reynolds number used by Schlatter et al. (2009)[17] at the inflow in the direct numerical simulations of a turbulent flow over a flat plate. A three-dimensional and a cross sectional shape of a two-dimensional trip are shown in Figs. 3(a) and (b), respectively. The undisturbed boundary layer profile at the trip location is also drawn in Fig. 3(b). The boundary-layer thickness at this location is about $\delta = 0.034\ m$. The ratio of the trip height to the boundary layer thickness is $k/\delta = 0.39$. The variation of the roughness Reynolds number $Re_{kk} = U_k\, k/\nu_k$, along the boundary layer height is shown in Fig. 3(c). The roughness Reynolds number for this roughness height $k = 0.0132$ is about 683. A critical value of $Re_{kk} = 600$ was suggested[3] based on experimental data for an effective trip. It will be observed later that even with this larger size trip, the boundary layer is not tripped in the simulation without any external forcing.

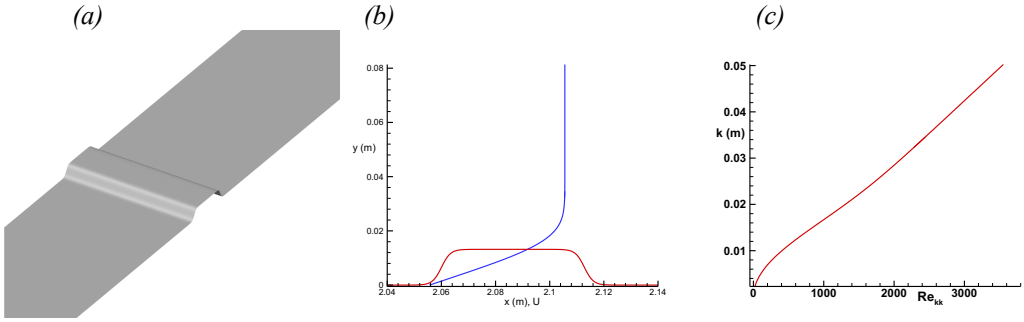

Fig. 3 The shape of a two-dimensional rectangular trip. (a) Three-dimensional view, (b) cross sectional view across the trip, and (c) variation of the roughness Reynolds number, Re_{kk}.

(c) Wavy trip

The shape of a sinusoidal wavy trip is generated by bending a two-dimensional rectangular rod into a sinusoidal form using the following equation.

$$h(x,z) = k\,\{0.5 - 0.5\tanh\{\sigma\,(r - r_0)/\Delta r\}\} \tag{6}$$

where

$$x_{01} = x_0 - A_{wave}\cos\left\{2.*\pi\,\frac{(z-\lambda/2)}{\lambda}\right\} \tag{7}$$

$$r = abs(x - x_{01}) \tag{8}$$

The amplitude of the wave shape is fixed by the constant A_{wave}. Simulations were performed for a roughness of $k = 0.0085\ m$, $r_0 = 0.039\ m$, and $\lambda = 0.039\ m$. The amplitude of the wave is selected to be $A_{wave} = 0.022\ m$. The mean center of the roughness is placed at $x_0 = 2.086\ m$. The smoothness parameters σ and Δr are selected to be 4 and $0.1r_0$, respectively. Simulations were performed with 4 waves to cover a spanwise domain size of 0.16 m. A three-dimensional and a cross sectional view of a wavy trip are shown in Figs. 4(a) and (b), respectively. The undisturbed boundary layer profile at the trip location is also drawn in Fig. 4(b). The roughness Reynolds number for this roughness height $k = 0.0085$ is about 300.

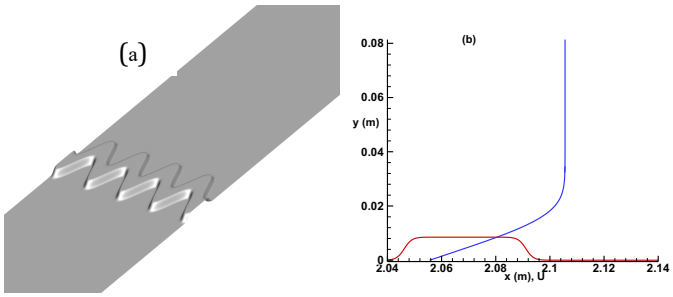

Fig. 4 The shape of a wavy trip: (a) three-dimensional view, and (b) cross sectional view across the trip.

III. Governing Equations

The partial differential equations solved are the three-dimensional unsteady compressible Navier-Stokes equations in conservation form. The viscosity is computed using Sutherland's law and the thermal conductivity is obtained from the Prandtl number ($Pr = 0.70$). A body-fitted curvilinear grid system was used in all simulations. The equations are transformed from the physical coordinate system (x, y, z) to the computational curvilinear coordinate system (ξ, η, ζ). The corresponding velocity components in those directions are (u, v, w), respectively. The velocities are nondimensionalized by the free stream velocity.

Solution Algorithm

The governing equations were solved using higher-order compact schemes with domain decomposition.[18, 19] Flow simulations were performed using a 6th-order compact scheme in all three directions. The order was reduced to 4th and 3rd order near the walls. A higher-order implicit filtering[17] of 8th-order was used in all three directions to remove the high wavenumber contents in the solution. A 3rd-order total-variation-diminishing (TVD) Runge-Kutta scheme was employed for time integration. The no-slip and constant temperature conditions are imposed at the flat plate surface. The wall temperature is fixed at 300K. Periodic conditions are applied in the spanwise direction. Characteristic boundary conditions are used at the outer boundary.

IV. Results

DNS with trips

Simulations are performed for two types of two-dimensional roughness trips and for one three-dimensional zig-zag trip. The shapes and the dimensions are described in the earlier section. Klebanoff et al.[2, 4] performed detailed experimental investigations of the mechanisms involved in two- and three-dimensional roughness induced transition in incompressible flows. It was concluded that two-dimensional roughness elements cause early transition to turbulent flow due to the destabilizing effects of inflectional profiles generated behind the roughness. Two-dimensional simulations are first performed without any external disturbances to identify the characteristics of the flow induced by a two-dimensional trip.

(a) Two-dimensional smooth hump

(1) Two-dimensional simulation

Two-dimensional simulations were first performed for the flow over the two-dimensional smooth hump. Figure 5 shows the u-velocity contours. The flow remained steady and did not have any separated region downstream of the trip. Figure 6 depicts the boundary layer profiles upstream and downstream of the trip center at different stations, x = 0.8, 0.95, 1.0, 1.05, 1.1, 1.25 (*-133k, -33k, 0k*, *33k, 67k, 167k*). Figure 6 also includes the unperturbed boundary layers at $x = 0.8$ and 1.25 m. It is seen that the boundary-layer profiles with and without the hump coalesce at these stations, $x = 0.8$ and 1.25 m. It is to be noted that the center of the hump is located at $x = 1$ m, and the half-width of the hump is 0.1 m. Hence the effects of the hump extend about two times the half-width upstream and about 2.5 times downstream. Another observation is that the boundary layer velocity profiles become fuller upstream and become inflectional downstream of the hump. This will have strong effects on the stability characteristics of the boundary layers upstream and downstream of the hump.

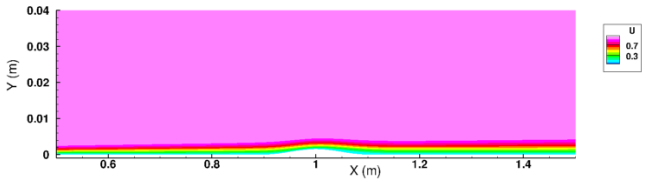

Fig. 5 *u*-velocity contours for flow over the two-dimensional hump.

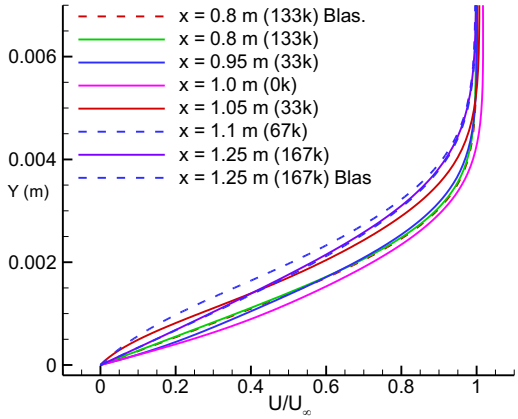

Fig. 6 Boundary-layer velocity profiles at upstream and downstream of the center of the hump.

A linear stability analysis was performed for the boundary layer profiles obtained with and without the hump. The growth rates and the N-Factors obtained from the stability analysis for several nondimensional frequencies, F, are presented in Figs. 7(a) and (b), respectively. The nondimensional frequency, F, is defined as

$$F = 2\pi f \frac{\nu_\infty}{U_\infty^2} \times 10^6 \tag{9}$$

Here f is the frequency in Hz, U_∞ is the freestream velocity, and ν_∞ is the kinematic frequency in the freestream. The growth-rate curves for the frequencies $F = 40$ and 60 show that boundary layers become stable upstream of the hump and unstable downstream of the hump compared to the unperturbed case. This is due to the previous observations in Fig. 6, i.e., the boundary layer profiles become fuller upstream of the hump and inflectional downstream compared to the unperturbed profiles. The maximum N-Factor obtained without the hump within the domain $x < 1.5\ m$ is about 4.5. The corresponding frequencies are about $F = 40 \sim 50$. The N-Factor curves with the hump display valleys across the hump before increasing to larger values downstream. The maximum N-factors are in the range of 6.5 for the frequencies $F = 40 \sim 60$.

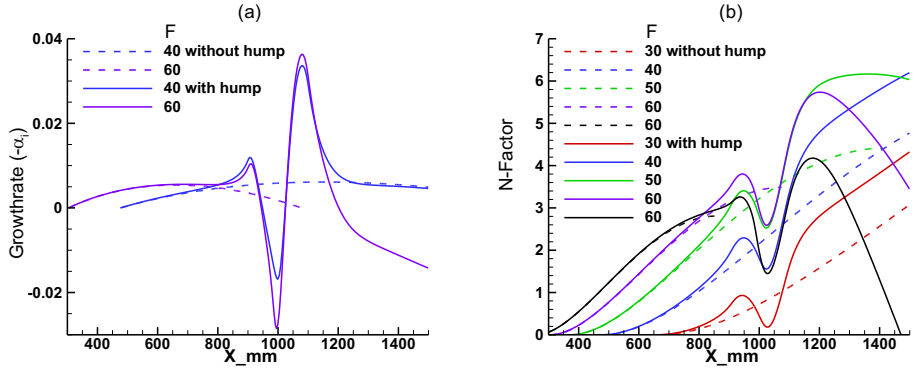

Fig. 7 (a) Growth rate and (b) N-Factor curves for different frequencies, *F*, without and with the hump.

After identifying the instability characteristics of the flow over the hump unsteady simulations were performed by applying a harmonic source through a narrow slit at the wall upstream of the hump. The unsteady wall normal velocity is given by

$$v(x, y = 0, t) = A_v \cos(\omega t) \exp\left(-\sigma \frac{(x-x_0)^2}{\Delta x^2}\right). \quad (10)$$

Here, A_v is the amplitude of the oscillations, ω is the frequency, x_0 is the location of the source, the parameters σ and Δx determine the width of the slit. The amplitude A_v is an important parameter in determining the transition location behind the trip. Simulations were performed for the frequency of $F = 60$ with amplitudes of $A_v = 0.00001$ and 0.00006. The unsteady disturbances were applied upstream of the trip at $x_0 = 0.5\ m$. Figures 8(a) and (b) display the instantaneous u-velocity contours generated by the blowing and suction applied at the wall upstream of the trip. Figures 9(a) and (b) display the evolution of the u-velocity along a grid line that is approximately located in the middle part of the boundary layer. Figures 8(a) and 9(a), as expected from the N-Factor curve, show that the perturbations for the low amplitude case $A_v = 0.00001$ initially grow and decay over the hump, and then grow again before decaying downstream. The maximum amplitude reached is about 0.01 and this occurs at about $x \sim 1.24m$. At the higher amplitude $A_v = 0.00006$, the initial growth of the disturbances is similar up to $x \sim 1.2m$. The amplitude reached at this station is about 0.027. However, downstream of this location the disturbances continue to grow instead of decaying as predicted from the linear instability calculations. This growth is due to the nonlinear effects. This was experimentally observed in the Klebanoff's[2] experiment and was also captured in the nonlinear PSE calculations[1].

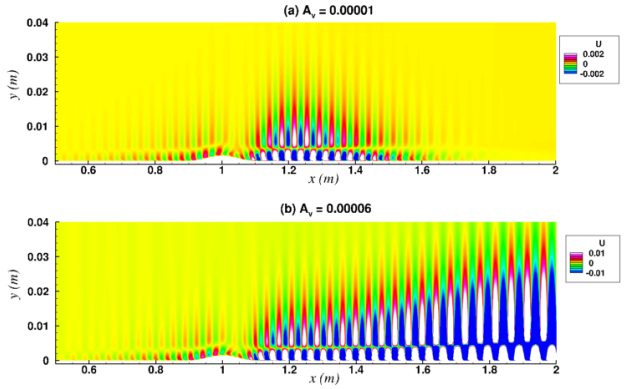

Fig. 8 Contours of the velocity field generated by the blowing and suction at the wall for the frequency $F = 60$ for flow over the two-dimensional hump (not to scale): (a) $A_v = 0.00001$, (b) $A_v = 0.00006$.

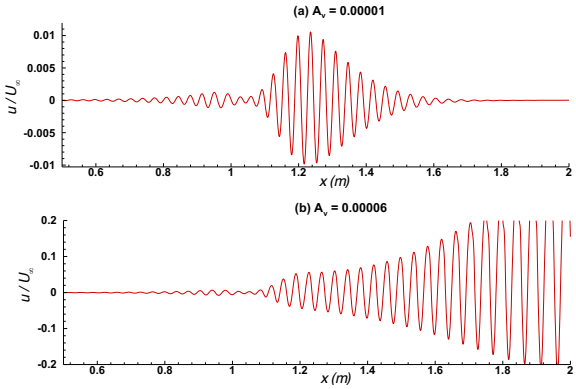

Fig. 9 Evolution of the velocity field in the middle part of the boundary layer in the streamwise direction for flow over the two-dimensional hump: (a) $A_v = 0.00001$, (b) $A_v = 0.00006$.

(2) Three-dimensional simulation

The previous linear stability analysis and the two-dimensional simulations showed that the trips make the boundary layer profiles more unstable and depending on the initial amplitudes of the instability waves, the disturbances can continue to grow downstream of the hump due to nonlinearity. The next important question is how does this unstable boundary layer break down to turbulence? One possible scenario is to investigate three-dimensional secondary instability[8] of the linear instability waves (primary instability) considered above.

In this section, simulations are performed to investigate the breakdown of the boundary layer over the hump due to subharmonic secondary instability mechanism. The unsteady normal velocity imposed at the wall is given by

$$v(x, y = 0, z,\ t) = \left\{A_v \cos(\omega t) + A_{2nd,subh}\, cos\left(\frac{\omega t}{2}\right)\, cos(\beta z)\right\}\ \exp\left(-\sigma \frac{(x-x_0)^2}{\Delta x^2}\right). \tag{11}$$

Here, ω is the frequency, β is the spanwise wavenumber of the secondary wave, A_v is the amplitude of the primary wave, and $A_{2nd,subh}$ is the amplitude of the secondary wave. The simulations are performed for a frequency of $F = 20$ and for a spanwise wavenumber of $\beta/Re_x \times 10^3 = 0.0911$. Here, Re_x is the local Reynolds number defined by $Re_x = \sqrt{U_\infty x/\nu_\infty}$. These parameters are the same as those used in Park et al.[4] The amplitudes of the input disturbances are $A_v = 0.00005$ and $A_{2nd,subh} = A_v/20$. The simulations are performed using a spanwise domain size of one spanwise wavelength and using 64 points in the spanwise direction.

Figure 10(a) shows the instantaneous u-velocity in the cross sectional view (x-y plane) at a fixed spanwise location $z = 0.02\ m$. Figures 10(b) and (c) depict the contours of the u-velocity and the w-velocity in the plan view along a fixed normal grid (j=20, $y \sim 0.0004\ m$), which is located a short distance above the plate. It is to be noted that the simulations are performed for one spanwise wavelength and the contours in Figs. 10(b) and (c) are plotted for two wavelengths for clarification using periodicity condition. The plan views, Figs. 10(b) and (c), display staggered patterns of velocity contours between $x \sim 1.3$ and $x \sim 1.5m$. These are the characteristic staggered patterns observed in the flow visualizations in laminar-turbulent transition caused by subharmonic instability mechanism.

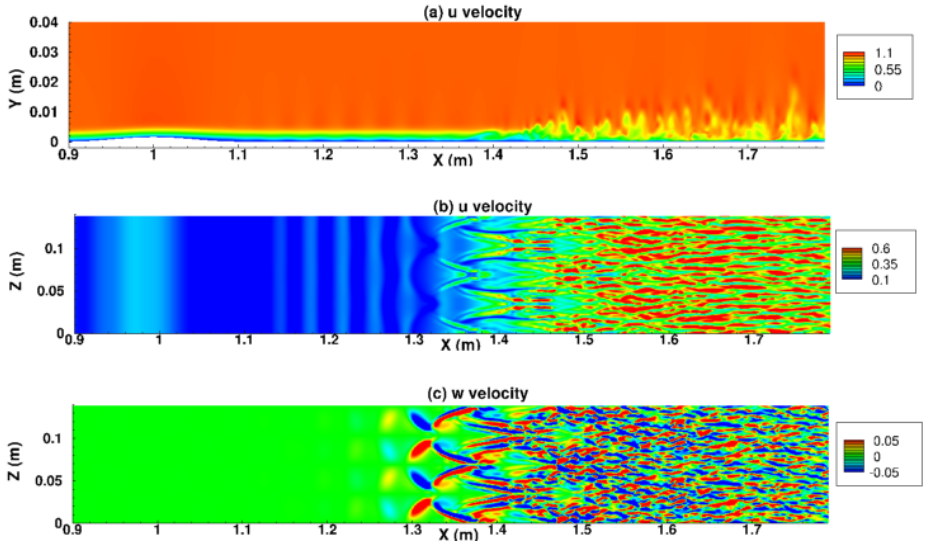

Fig. 10 Instantaneous contours of (a) *u*-velocity in the (*x*-*y*) plane (not to scale), (b) *u*-velocity, and (c) *w*-velocity in the (*x*-*z*) plane at *y* = 0.0004 *m* for flow over the two-dimensional hump.

Assuming the flow field is periodic in time and in spanwise direction, the velocity field is decomposed into different Fourier modes in frequency and in spanwise wavenumber as given below.

$$u(x, y, z, t) = \sum_{m=-M}^{M} \sum_{n=-N}^{N} u_{mn}\,(x, y)\, e^{i(n\beta z - m\omega t)} \tag{12}$$

The amplitude function $u_{mn}(x, y)$ represents the amplitude of the mode (m, n), which has a frequency $m\omega$ and a spanwise wavenumber $n\beta$. Note that omega in Eq. (12) is now the subharmonic frequency for the subharmonic breakdown and not the primary frequency as defined in Eq. (11). Figure 11 shows the variations of the amplitude of

different modes u_{20}, u_{11}, u_{40}, and u_{31}. u_{20} is the primary mode and u_{11} is the secondary subharmonic mode. The other modes are generated by the nonlinear interactions of different modes. Figure 11 displays the classical mode diagram for a subharmonic induced transition process in a boundary layer. When the amplitude of the primary wave reaches a value of 0.0033, the secondary instability sets in and the amplitude of the secondary wave, u_{11}, increases steeply. After that, due to nonlinear interactions, higher modes are generated and the flow transitions into a turbulent flow. Figure 12 shows the variation of the time averaged skin friction coefficient along the x-direction. The empirical skin friction relation with the Reynolds number for a zero pressure gradient turbulent boundary layer, $cf = 0.027\ (Re_x)^{-1/7}$, is also plotted in the figure.

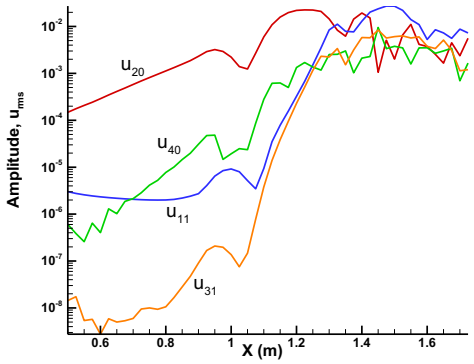

Fig. 11 Variation of the amplitudes of different modes.

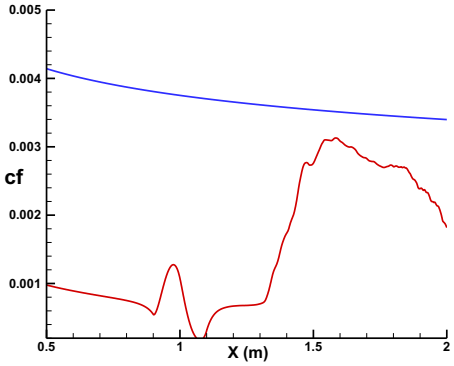

Fig. 12 Variation of the mean skin friction along with the empirical turbulent *cf*.

(b) Two-dimensional rod

(1)Two-dimensional results

Two-dimensional simulations were performed for the flow over a two-dimensional rectangular trip. The parameters are given in the previous section. The flow remained steady and created a long separated region downstream of the trip. Figure 13 shows the *u*-velocity contours. The separated region is shown as the gray area in the figure. The flow separates at the top of the trip and reattaches close to $x \sim 2.66\ m$, which is about 45 trip heights behind the trip. Figure 14 depicts the boundary-layer profiles downstream of the trip at different stations, $x = 2.2$, 2.4, 2.7, and 3.0 m ($9k$, $24k$, $45k$, $69k$). Guided by Klebanoff's[2] findings that wave-like disturbances are continuously shed from the trip, a linear stability analysis was performed for the boundary layer profiles downstream of the trip to detect the origin of these waves. The N-Factors obtained from the stability analysis are presented in Fig. 15 for the most amplified frequencies of 150, 200, 300, and 400 *Hz*. The N-factors are in the range of 8 for these frequencies and the maximum N-Factor of 8.5 is reached for the frequency of 200 *Hz*.

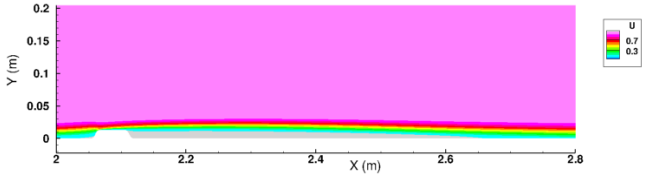

Fig. 13 *u*-velocity contours and the separated region for flow over the two-dimensional rectangular rod.

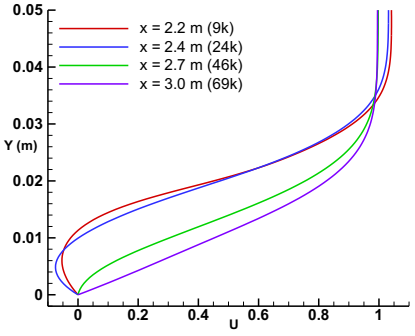

Fig. 14 Boundary-layer velocity profiles at different stations.

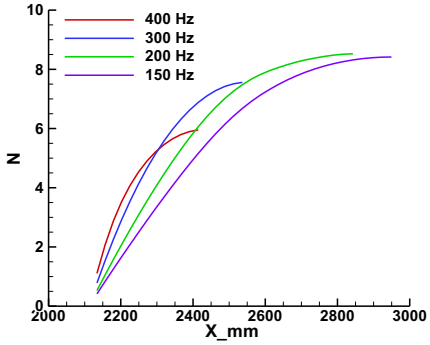

Fig. 15 N-Factor curves for different frequencies.

After identifying the instability characteristics of the separated region behind the trip, unsteady two-dimensional simulations were first performed by applying a harmonic source through a narrow slit at the wall upstream of the trip. The expression used for the harmonic source is given in Eq. (10). The amplitude A_v is an important parameter in determining the transition location behind the trip. Simulations were performed for the most amplified frequency of 200 *Hz* with an amplitude of $A_v = 0.0002$. The unsteady disturbances were applied upstream of the trip at $x_0 = 1.8\ m$. Figure 16 shows the instantaneous velocity contours of the perturbations generated by the blowing and suction applied at the wall upstream of the trip. It is seen that as in the experiment the external forcing initiates the instability waves inside the recirculation zone. The maximum perturbation amplitude reached in this case is about 0.11. This occurs at a distance of $x \sim 2.73\ m$ and at a height of $y \sim 0.0033\ m$. The trip height is $0.0132m$. This shows that the disturbances are confined very close to the wall at a height of 25% of the trip height. Figure 17 displays the evolution of the *u*-velocity along a grid line (j=12, y=$0.0058m$) that is approximately located at 40% of the trip height. The disturbances grow up to $x \sim 3m$ and then decay . In the smooth hump case at high amplitude, the disturbances continue to grow due to nonlinearity.

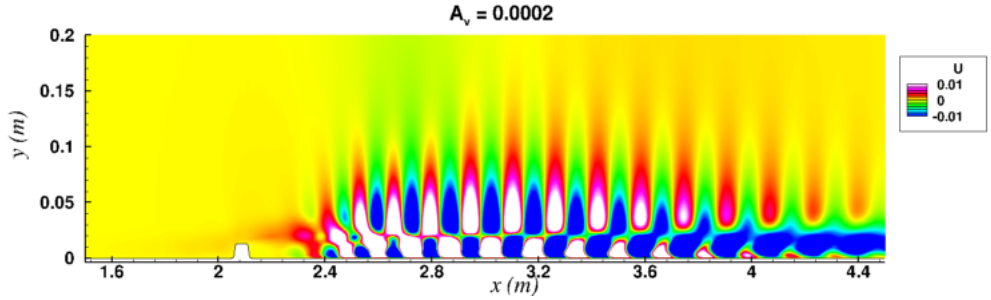

Fig. 16 Contours of the *u*-velocity field generated by the blowing and suction at the wall for flow over the two-dimensional rectangular rod.

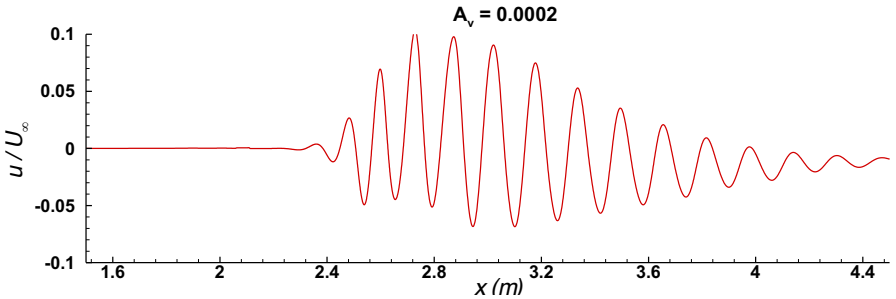

Fig. 17 Streamwise evolution of the *u*-velocity field in the middle part of the boundary layer in the streamwise direction.s

(2) Three-dimensional simulation

The next step was to investigate the breakdown of these two-dimensional disturbances into a three-dimensional turbulent flow. As described earlier, different secondary instability breakdown mechanisms are investigated: fundamental and subharmonic type breakdown mechanisms and oblique mode type breakdown mechanism where two symmetric oblique modes are introduced upstream of the trip. Oblique mode type breakdowns have been investigated in incompressible boundary layers[14, 16] and in compressible boundary layers[13, 15] and found to be more efficient in causing early transition in compressible boundary layers.

For simulations over the rectangular trip, the unsteady normal velocity imposed at the wall for the (a) fundamental, (b) subharmonic, and (c) oblique type breakdown mechanisms is given below.

(a) Fundamental secondary instability

$$v(x, y = 0,\ z, t) = \left\{A_v \cos(\omega t) + A_{2nd,fund}\, cos(\omega t)\, cos(\beta z)\right\}\ \exp\left(-\sigma \frac{(x-x_0)^2}{\Delta x^2}\right). \quad (13)$$

(b) Subharmonic secondary instability

$$v(x, y = 0, z, t) = \left\{A_v \cos(\omega t) + A_{2nd,subh}\, cos\left(\frac{\omega t}{2}\right)\, cos(\beta z)\right\}\ \exp\left(-\sigma \frac{(x-x_0)^2}{\Delta x^2}\right). \quad (14)$$

(c) Oblique mode breakdown

$$v(x, y = 0, z, t) = \left\{\qquad\qquad A_{2nd,obl}\, cos(\omega t)\, cos(\beta z)\right\}\ \exp\left(-\sigma \frac{(x-x_0)^2}{\Delta x^2}\right). \quad (15)$$

The amplitudes of the input disturbances are A_v = 0.0002, $A_{2nd,fund} = A_{2nd,subh} = A_v/10$, and $A_{2nd,obl}$ = 0.001. The simulations were performed for a frequency of f = 200 *Hz* and for a spanwise wavelength of 0.15 *m*. Simulations are performed using a spanwise domain size of one spanwise wavelength and using 64 points in the spanwise direction.

For the fundamental breakdown scenario, Fig. 18(a) shows the instantaneous *u*-velocity in the cross sectional view (*x*-*y* plane) at a fixed spanwise location *z* = 0.075 *m*. Figures 18(b) and (c) depict the contours of the *u*-velocity and the *w*-velocity in the plan view along a fixed normal grid (*j*=12, *y* ~ 0.0058 *m*), which is located a short distance above the plate. The plan views, Figs. 18(b) and (c), display aligned patterns of velocity contours between *x* ~ 2.8 and *x* ~ 3.4*m*. These are the characteristic aligned patterns observed in the flow visualizations in laminar-turbulent transition caused by the fundamental instability mechanism. Figure 19 shows the variations of the amplitude of different modes u_{10}, u_{11}, u_{20}, and u_{02}. u_{10} is the primary mode and u_{11} is the secondary mode. The other modes are generated by the nonlinear interactions of different modes. The mode u_{02} is a steady streak mode generated by the interaction of secondary modes. Figure 20 shows the variation of the time averaged skin friction coefficient along the *x*-direction. The empirical skin friction relation with the Reynolds number for a zero pressure gradient turbulent boundary layer, $cf = 0.027\ (Re_x)^{-1/7}$, is also plotted in the figure.

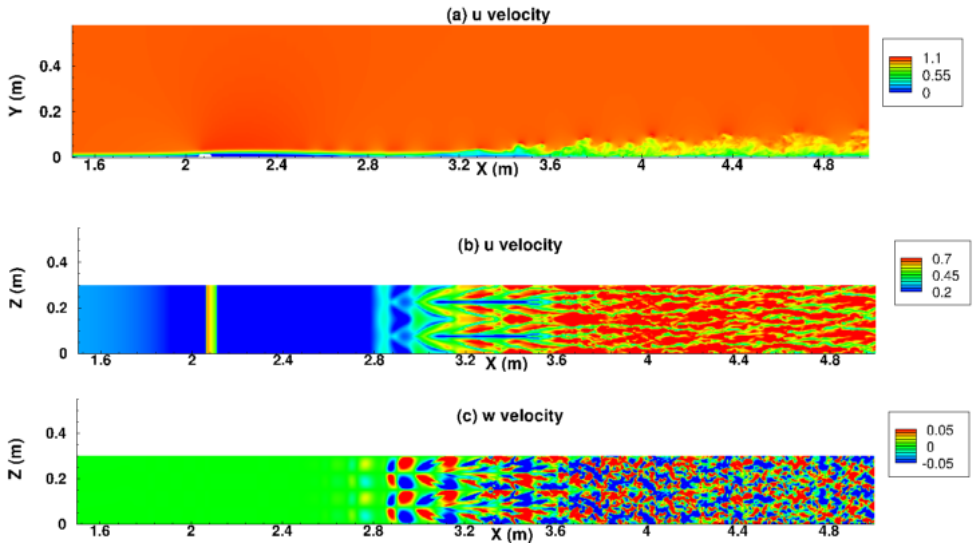

Fig. 18 Instantaneous contours of (a) *u*-velocity in the (*x*-*y*) plane, (b) *u*-velocity, and (c) *w*-velocity in the (*x*-*z*) plane at *y* = 0.0058 *m*. Fundamental breakdown for flow over the two-dimensional rectangular rod.

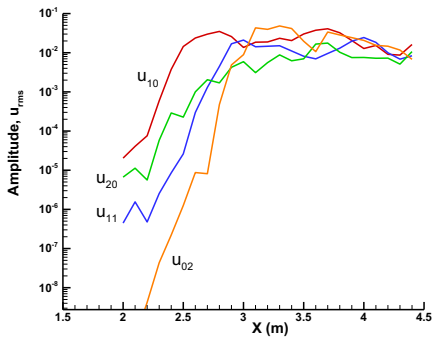

Fig. 19 Variation of the amplitudes of different modes.

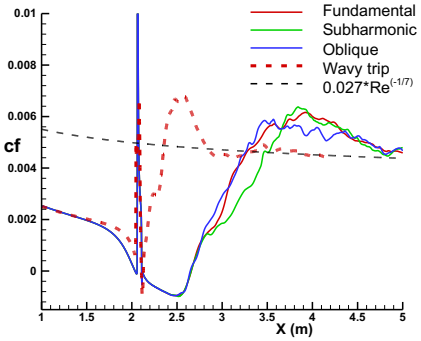

Fig. 20 Variation of skin friction.

Similarly, Figs. 21 and 22 depict the results for the subharmonic type breakdown. The results are similar to the smooth hump case presented earlier. The staggered contour patterns are observed between $x \sim 2.8$ and $x \sim 3.6m$. The growth of different modes is displayed in Fig. 22. The secondary mode u_{11} starts to grow from $x \sim 2.4m$. The amplitudes of the primary and the secondary modes reach equal amplitudes close to $x \sim 3m$. The variation of the time averaged skin friction coefficient for this case is shown in Fig. 20. The skin friction starts to deviate from the laminar value close to $x \sim 2.5m$ and grows strongly downstream. It overshoots the expected turbulent skin friction curve and then decreases towards the expected value farther downstream.

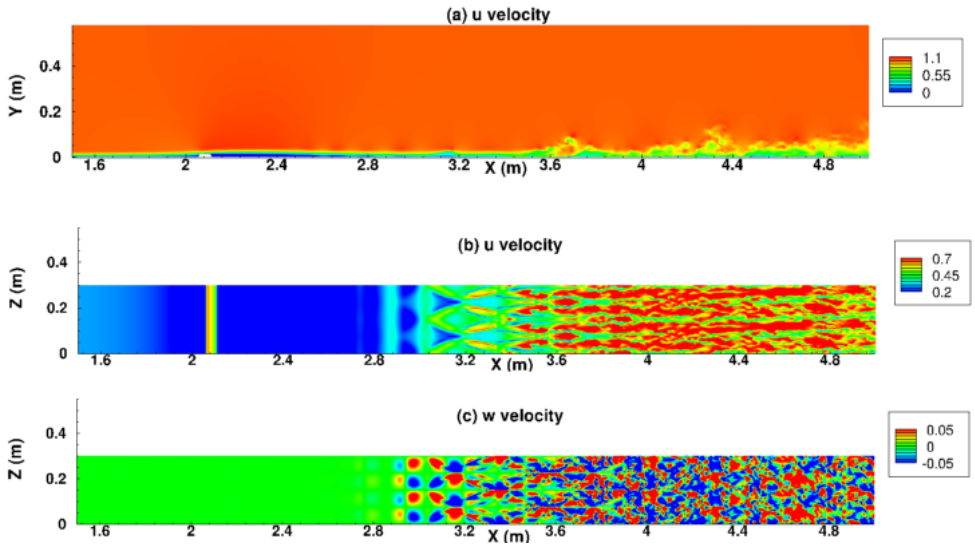

Fig. 21 Instantaneous contours of (a) *u*-velocity in the (*x*-*y*) plane, (b) *u*-velocity, and (c) *w*-velocity in the (*x*-*z*) plane at *y* = 0.0058 *m*. Subharmonic breakdown.

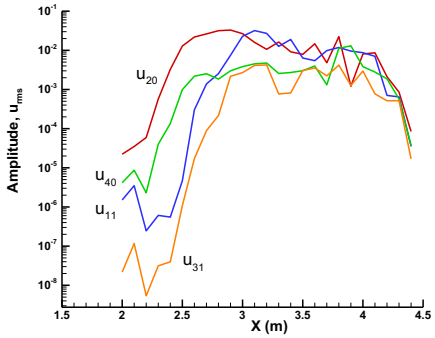

Fig. 22 Variation of the amplitudes of different modes.

Simulations of the of the oblique breakdown were performed for the same frequency f = 200 Hz and for the same spanwise wavelength of 0.15*m*. The amplitude of the input disturbance is $A_{2nd,obl}$ = 0.001. This amplitude is five times higher than the amplitude used for the primary wave in the fundamental and subharmonic type breakdown cases. At smaller forcing amplitudes, nonlinear development and breakdown to turbulence did not occur. Figure 23 shows the contours of the *u*-velocity and the *w*-velocity in the cross sectional and the spanwise planes as shown in the previous cases. The time averaged skin friction coefficient is plotted in Fig. 20. The skin friction coefficient overshoots the equilibrium value for a flat plate and approaches the expected value slowly downstream. It is seen that even though the transition mechanisms are different, the skin friction distributions are almost the same. The slow recovery towards the equilibrium value after the peak value appears similar for all the cases.

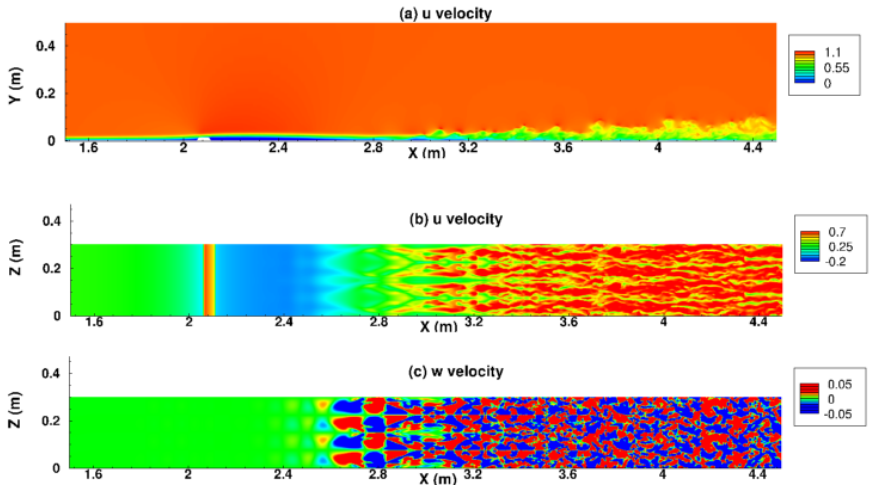

Fig. 23 Instantaneous contours of (a) *u*-velocity in the (*x*-*y*) plane, (b) *u*-velocity, and (c) *w*-velocity in the (*x*-*z*) plane at *y* = 0.0058 *m*.

(c) Wavy trip

Simulations were performed with a wavy trip with a spanwise domain size of 0.16*m*. The dimensions of the trip are given in the previous section. The roughness Reynolds number is about Re_{kk} = 300. Figure 24 displays the instantaneous isosurfaces of the second invariant of the velocity gradient tensor at Q = 0.25. The isosurfaces are colored by the local *u*-velocity. Figure 25(a) shows the instantaneous *u*-velocity in the cross sectional view (*x*-*y* plane) at a fixed spanwise location *z* = 0.02 *m*. Figures 25(b) and (c) depict the contours of the *u*-velocity and the *w*-velocity in the plan view along a fixed normal grid (*j*=20, *y* ~ 0.004 *m*), which is located a short distance above the plate. Figure 26 shows the evolution the *u*-velocity in the middle part of the boundary layer (*y* ~ 0.01 *m*) along the streamwise direction at a constant spanwise location *z* ~ 0.02 *m*. Simulation results reveal that a three-dimensional recirculation zone forms immediately downstream of each wave. This recirculation region exists up to *x* ~ 2.3 *m*. Downstream of this region, a low speed streaks develops. Figure 26 shows that unsteady fluctuations start to develop in this region. The amplitude of these fluctuations grows and reaches a large value by *x* ~ 2.6 *m*. Associated with the oscillations, hairpin vortices appear downstream of each wave. These hairpin vortices convect downstream and grow in size. These vortices finally merge and break down into a turbulent flow. The time averaged skin friction is shown in Fig. 20 and is compared with the skin friction curves obtained under different transition scenarios with the two-dimensional rectangular rod. The results show that the flow becomes turbulent much earlier with the zig-zag trip compared to the rectangular rod without any external forcing. However, it should be noted that the forcing amplitude is 5 times larger in the oblique mode case than the forcing amplitudes used in the other scenarios.

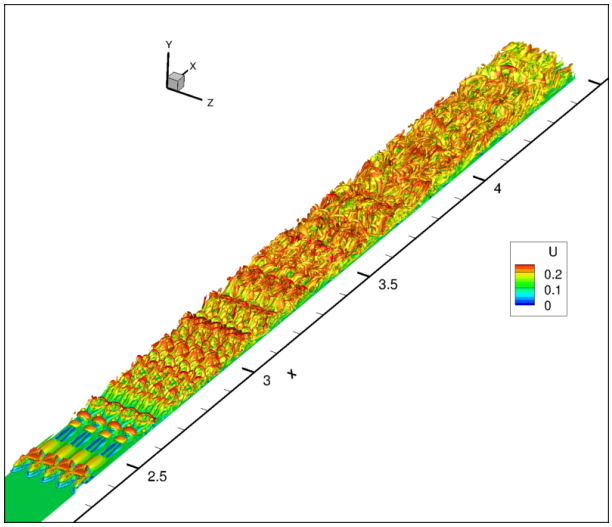

Fig. 24 Instantaneous iso-surfaces of Q = 0.25 and are colored by the local *u*-velocity for the wavy trip.

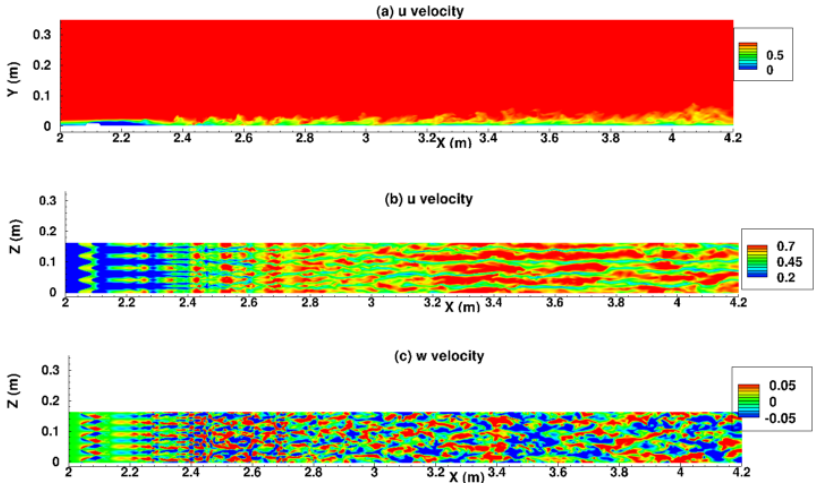

Fig. 25 Instantaneous contours of (a) *u*-velocity in the (*x*-*y*) plane, (b) *u*-velocity, and (c) *w*-velocity in the (*x*-*z*) plane at *y* = 0.004 *m* for the wavy trip.

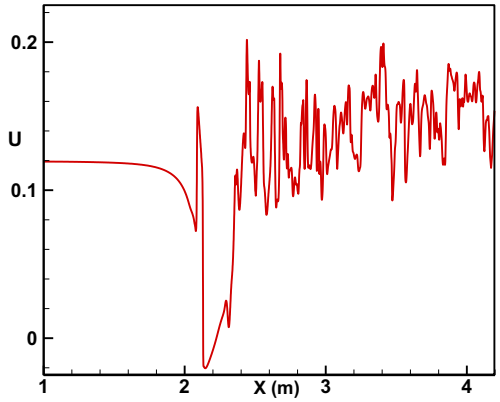

Fig. 26 Evolution of the *u*-velocity field in the middle part of the boundary layer (*y* ~ 0.01 *m*, *z* = 0.02 *m*) in the streamwise direction.

V. Conclusions

DNS were performed for flows over a flat plate to investigate the mechanisms that promote the flow behind boundary layer transition trips transitioning to a turbulent flow. Simulations were performed with a two-dimensional smooth hump, a two-dimensional rectangular rod trip, and a three-dimensional zig-zag wavy trip. The corresponding Reynolds numbers based on the roughness heights are Re_{kk} = 760, 683, and 300, respectively. For all the cases considered, steady mean flows were obtained. Linear stability analysis was performed to determine the stability characteristics of the boundary layers generated by the trips. After identifying the most amplified frequencies, two- and three-dimensional simulations were performed to investigate the breakdown of the boundary layers induced by the trips. Several three-dimensional secondary instability mechanisms, fundamental, subharmonic, and oblique mode types, were simulated to identify effectiveness of different mechanisms in promoting early transition behind the trips.

Simulations with a two-dimensional smooth hump showed that the mean boundary layer profiles become fuller upstream of the hump and become inflectional downstream. Due to these modifications to the mean flow, the boundary layers become stable upstream and strongly unstable downstream compared to the unperturbed case. The stabilization of the flow upstream of the hump reduces the overall effectiveness of the hump in destabilizing the boundary layer. The net increment in the overall growth, N-Factor, increased by a modest value of 2.5. The two-dimensional simulations with a small harmonic forcing amplitude agreed with the linear stability predictions. However, at higher

forcing amplitude, evolution of the disturbances deviates from the linear stability predictions and continues to grow downstream of the neutral point. These findings agree with the linear and nonlinear PSE calculations[1] and the experimental observations of Klebanoff et al.[2] Three-dimensional disturbances with a subharmonic input showed subharmonic secondary instability is a possible mechanism in causing the flow to become turbulent.

Simulations for the two-dimensional rectangular rod trip without any external forcing produced a steady flow field with a long recirculation zone behind the roughness. Linear stability analysis showed that the recirculation zone is strongly unstable for a range of frequencies 100 ~ 300 *Hz*. The maximum N-Factors obtained are in the range of 8 to 8.5. Simulations with a harmonic forcing at a frequency of 200 *Hz* captured the expected strong growth of unsteady disturbances in the recirculation zone. The maximum disturbance amplitudes occur very close to the wall and well below the roughness height. Three-dimensional simulations were performed to investigate the breakdown of these two-dimensional disturbances into a turbulent flow. Three different types of secondary disturbances, fundamental, subharmonic, and oblique types, were used in the simulations. The input amplitudes of the harmonic source are very small on the order of 0.02% for the primary wave and 0.002% for the secondary wave. In the oblique mode type breakdown simulation, a larger value on the order of 0.1% is required to force the transition for the oblique mode. The simulation results showed all three mechanisms could lead to breakdown.

Simulations were then performed with a sinusoidal wavy tape trip. The results showed a recirculation zone behind each wavy trip. Downstream of this recirculation region, a low speed streak was formed. Unsteady perturbations started to develop in this region. These disturbances grew in amplitude and finally saturated at large values. Associated with unsteady oscillations, hairpin vortices were shed behind the wavy trip. These hairpin vortices convected downstream and grew in size. Finally, these vortices merged, and the flow developed into a turbulent state. The skin friction evolution revealed that zig-zag trip is more efficient in tripping the boundary layer compared to rectangular trips. It was also found that the zig-zag tape did not require any external forcing to cause early transition compared to the two-dimensional trip cases.

Acknowledgment

This work was supported by the NASA Transformational Tools and Technologies (TTT) project of the Transformative Aeronautics Concepts Program.

References

[1]Park, D., and Park, O. S., "Linear and non-linear stability of incompressible boundary layer over a two-dimensional hump", Computers & Fluids, 73 (2013) 80-96.
[2]Klebanoff, P. S., and Tidstrom, K. D., "Mechanisms by which a Two-Dimensional Roughness Element Induces Boundary Layer Transition," Phys. Fluids 15, 1972, pp. 1173-1188.
[3]Braslow, A. L., and Knox, E. C., "Simplified Method for Determination of Critical Height of Distributed Roughness Particles for Boundary-Layer Transition at Mach Numbers from 0 to 5", NACA Technical Note 4363, 1958.
[4]Klebanoff, P. S., Cleveland, W. G., and Tidstrom, K. D., "On the Evolution of a Turbulent Boundary layer Induced by a Three-dimensional Roughness Element," J. Fluid Mech. (1992), vol. 237, pp. 101-187.
[5]Tani, I., "Boundary-Layer Transition," Annu. Rev. Fluid Mech. 1969.1:169-196.
[6]Acarlar, M. S., and Smith, C. R., "A Study of Hairpin Vortices in a Laminar Boundary Layer. Part 1. Hairpin Vortices Generated by a Hemisphere Protuberance," J. Fluid Mech. (1987), vol. 175, pp. 1-41.
[7]Wu, Xiaohua, "Inflow Turbulence Generation Methods", Annual Review of Fluid Mechanics, 2017, 49, 23-49.
[8]Herbert, T., "Secondary Instability of Boundary Layers", Ann. Rev. Fluid Mech. 1988. 20:487-526.
[9]Herbert, T., "Parabolized Stability Equations", Annu. Rev. Fluid. Mech, 1997, 29:245-83.
[10]Chang, C.-L., Malik, M. R., Erlebacher, G., and Hussaini, M. Y., "Compressible Stability of Growing Boundary Layers using Parabolized Stability Equations", AIAA Paper No. 91-1686 (1991)
[11]Fasel, H. F., Rist, U., and Konzelmann, U., "Numerical Investigation of the Three-Dimensional Development in Boundary-Layer Transition", AIAA J. , Vol. 28, No. 1, January 1990.
[12]Joslin, R. D., Streett, C. L., and Chang, C. L., "3-D spatial Direct Numerical Simulation Code Validation Study-A comparison with LST & PSE Theory for Boundary-Layer Transition on a Flat Plate", NASA TP, March 1992.
[13]Chang, C.-L., and Malik, M. R., "Oblique-mode breakdown and secondary instability in supersonic boundary layers", J. Fluid Mech. (1994), vol. 273, pp. 323-360.
[14]Joslin, R. D., Streett, C. L., and Chang, C.-L., "Oblique-wave breakdown in an incompressible Boundary Layer Computed by Spaptial DNS and PSE Theory", Instability, Transition and Turbulence, Springer-Verlag, 1992, M.Y. Hussaini et al, (eds).
[15], C. S., Wernz, S., and Fasel, H. F., "Investigation of Oblique Breakdown in a Supersonic Boundary Layer at Mach 2 using DNS", AIAA Paper No. 2007-949, 2007.
[16]King, R. A., and Breuer, K., "Oblique transition in a laminar Blasius boundary layer", J. Fluid Mech. (2002), vol. 453, pp. 177-200.

[17]Schlatter, Orlu, R, Li, Q., Brethouwer, G., Fransson, H. H. M., Johanson, A. V., Alfredsson, P. H., and Henningson, D. S., "Turblent boundary layers up to $Re_\theta = 2500$ studied through simulation and experiment", Phys. Fluid 21, 051702 (2009).
[17]Lele, S. K., "Compact Finite Difference Schemes with Spectral-like Resolution," *J. Comut. Phys*., Vol. 103, 16 (1992).
[18]Visbal, M. R., and Gaitonde, D. V., "On the Use of Higher-Order Finite-Difference Schemes on Curvilinear and Deforming Meshes", *J. Compu. Phys*., Vol. 181, 2002, pp. 155-185.